Research Article Vol. 40, No. 9 / September 2023 / Journal of the Optical Society of America A 1789

Journal of the Optical Society of America A
OPTICS, IMAGE SCIENCE, AND VISION

Computational analysis of a scalable optically homogeneous free-space interferometer

Aaron J. Pung

Slingshot Aerospace, 841 Apollo St #350, El Segundo, California 90245, USA (aaron.pung@gmail.com)

Received 25 May 2023; revised 10 August 2023; accepted 18 August 2023; posted 21 August 2023; published 30 August 2023

This study describes a scalable optically homogeneous free-space interferometer. Computationally modeled as an unbroken block of fused silica, the interferometer's six-sided design is simple and intuitive, exploiting total internal reflection and refraction to split and recombine a collimated input beam. During propagation, one portion of the split beam remains within the substrate to act as a reference beam. The second portion of the split beam is exposed to the surrounding environment, enabling real-world environment characterization in real time. Validation of the interferometer concept is performed using numerical and analytical techniques. Based on its scalability and robustness, the proposed interferometer design is primed for applications in atmospheric sensing, passive chemical detection, and spaceborne technologies. © 2023 Optica Publishing Group

https://doi.org/10.1364/JOSAA.496379

1. INTRODUCTION

The high degree of precision offered by optical interferometry has proven vital in characterizing vibrations, assessing surface topology, and measuring refractive indices. In the latter case, the ability to quickly and accurately assess real-world environments heavily relies on being able to continuously sample the surrounding atmosphere. In the past, gas chemistry characterization has been performed using classical Rayleigh and Mach–Zehnder interferometers. Using the method of Lord Rayleigh [1,2], for instance, a gas specimen is captured and placed in one arm of a two-arm interferometer system. The insertion of the gas specimen creates a difference in optical path length (OPL) between the reference and probe beams, ultimately allowing the refractive index of the sample to be determined for different wavelengths. At the same time, isolating the gas sample from its environment ensures the sample no longer experiences variations seen in nature. For this reason, the conventional Rayleigh interferometer and similar table-top systems are rendered useless in performing real-time measurements of real-world environments.

To overcome these limitations, interferometers based on optical fiber have gained popularity due to their small footprint, low weight, high sensitivity, flexibility, portability, and immunity to electromagnetic interference [3–6]. Unfortunately, fiber-based interferometers are often plagued by a number of drawbacks, including a lack of versatility and modularity, coupling loss, and unfamiliarity to the end user [7]. Additionally, fiber-based systems are limited by their material composition and geometry, since these factors directly limit the wavelengths that can efficiently propagate within the fiber [8]. The same optical fiber used to transmit and receive light at 600 nm will not be able to do so at 6000 nm [9].

Free-space interferometer systems provide another alternative [10–17]. Lighter than table-top systems and more robust than optical fiber, monolithic systems exploit material and mechanical properties of their configuration to reduce issues that may arise during fabrication. While forming a monolithic structure from an unbroken block of material avoids the need to align and bond separate components [18,19], the align-and-bond technique tends to be more prevalent in the literature [12,14–17]. By removing detached or rotating mirrors, the cosine error due to inconsistencies in mirror position of monolithic structures is significantly reduced [10,12,14,16], improving overall alignment and experiment repeatability. Four examples of previously reported monolithic interferometers are illustrated in Fig. 1.

Although monolithic free-space systems typically enjoy many advantages, scaling is not one of them. Enlarging each geometry in Fig. 1, for example, would also require expanding, moving, or re-aligning at least one other component in addition to the main body. Furthermore, existing free-space designs are overly complex since each structure relies on the presence of more than one component to form an interferogram. As the proposed design illustrates, this need not be the case.

A more simple and intuitive approach is to tailor the geometry of a homogeneous and monolithic slab of optically transparent material to naturally split and recombine an incident light source. Without the need to align and bond multiple components, the design becomes highly scalable and highly dependent on the mechanical, chemical, and optical properties of its substrate. For instance, a monolithic interferometer comprising fused silica benefits from the material's high softening point,

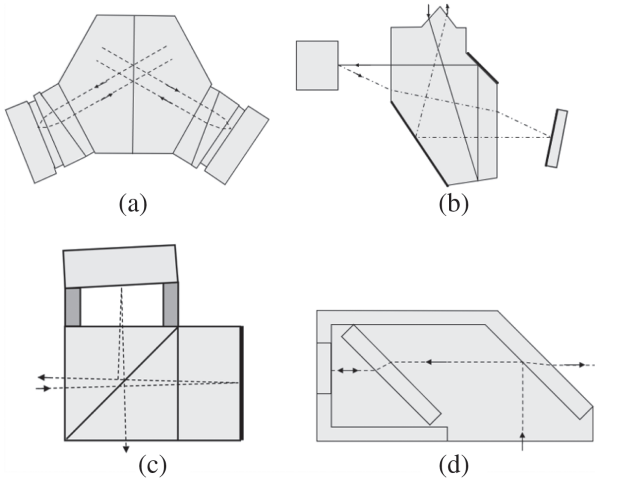

Fig. 1. Previously reported monolithic interferometers including a (a) robust monolithic ultraviolet interferometer [12], (b) monolithic micro-optical interferometer [19], (c) monolithic interferometer for fringe imaging [14], and (d) monolithic interferometer for FT-IR spectroscopy [11].

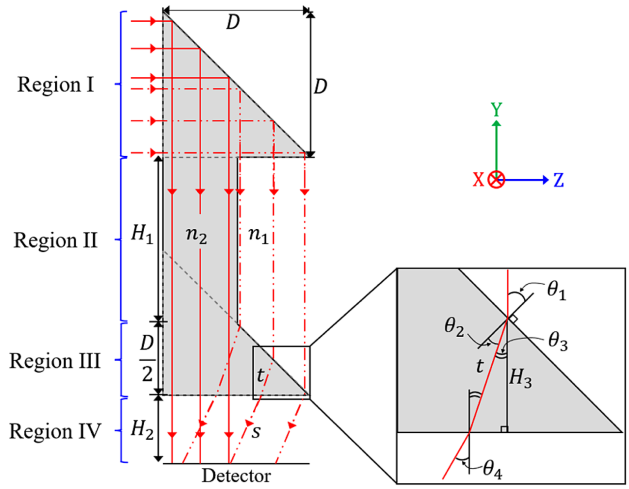

Fig. 2. SOHFI geometry is illustrated. The inset further details optical parameters of the structure.

resistance to radiation and thermal shock, low thermal expansion, high chemical purity, and strong transmission across the UV, VIS, and NIR regimes. Alternatively, a monolithic interferometer comprising calcium fluoride would benefit from a wider transmission band (>90% optical transmission from 200–7000 nm), but would also suffer from higher mechanical fragility.

Embodying this simplified approach, the scalable optically homogeneous free-space interferometer (SOHFI) proposed in this study takes the form of a six-sided monolith comprising fused silica. Similar to the Mach–Zehnder interferometer, an incident beam entering the device is split into a reference and probe beam. As the two beams propagate, the reference beam remains contained within the structure while the probe beam is briefly exposed to the surrounding environment. A slanted surface near the base of the SOHFI recombines the reference and probe beams to form an oblique interferogram.

Generally speaking, the SOHFI represents one component in a larger system; to be fully operational, a collimated coherent source and detector are also needed. The interferogram formed by the structure can be recorded and continuously monitored on the detector, enabling timely recognition of changes in the refractive index of a surrounding environment. For brevity, detailed discussions on fringe counting [20–23], refractive index measurements [24–26], and interferometric analysis will not be presented here given their prevalence in the literature.

2. GEOMETRY AND OPERATION

The side profile of the proposed SOHFI design is illustrated in Fig. 2, overlaid with a simple ray trace to show the flow of light through the structure. For clarity of discussion, the SOHFI has been divided into four regions (I, II, III, and IV). Separated by a width $D/2$, the two vertical faces of the structure are parallel to each other and the x-y plane. The horizontal face at the bottom of the structure is parallel to the detector and the x-z plane. The slanted faces in regions I and III are tilted at 45° with respect to the x-y plane, and the geometry of the structure is constant in the x direction. To eliminate stray reflections, each face of the SOHFI is coated with an ideal broadband anti-reflection coating.

In the most general case, the SOHFI structure comprises a material with refractive index n_2 and is surrounded by an environment with refractive index n_1. The isosceles right triangle of side length D in region I is identical to another isosceles right triangle beginning in region II and terminating at the bottom of region III; both triangles are outlined with a gray dashed line. Regions I and III are separated by a column of material with height H_1. The column intersects the upper half of the lower isosceles right triangle at a height $D/2$ from the bottom of the structure, defining region III.

In operation, collimated light from a coherent source traveling in the $+z$ direction enters the SOHFI structure in region I. After passing through the entry face, the incident rays strike the slanted surface of region I and are directed downward ($-y$) via total internal reflection (TIR). Upon reaching region II, the incident light is naturally split by the body of the interferometer. Based on the width of the SOHFI in this region, half the rays remain within the structure to act as a reference beam while the remaining half travel outside the structure as a probe beam. Similar to a Mach–Zehnder interferometer, the probe beam passes through the external environment and experiences a phase shift relative to the reference beam. Unlike the Mach–Zehnder interferometer, the probe beam passing through the surrounding environment allows the SOHFI to make real-world measurements in real time. The reference and probe beams are recombined in regions III and IV via refraction of the probe beam through the slanted surface in region III.

The same slanted surface introduces additional complexity because the OPL of the probe beam varies based on its proximity to the SOHFI structure. For instance, probe rays traveling close to the structure will immediately refract back into the monolith after traversing region II, while rays farther from the structure continue traveling through the open environment before refracting back into the structure. The variation in OPL in region III creates an additional phase difference between the reference and probe beams. When the two beams recombine,

their cumulative phase difference gives rise to the familiar light and dark fringes of an interferogram.

Due to the geometric simplicity of the SOHFI, an analytical description of the total OPL of the reference beam (OPL_R) and probe beam (OPL_P) are derived below, followed by numerical validation of the SOHFI concept.

3. THEORETICAL ANALYSIS

Based on the geometry of region I, any ray entering the SOHFI orthogonal to the left-most edge will traverse a fraction f of the triangle's side length D before striking its hypotenuse. Assuming $n_2 > n_1$, rays at the interface undergo TIR and are redirected downward along the $-y$ direction. Following TIR, the same ray will traverse a distance $(1-f)\cdot D$ from the hypotenuse to the bottom of region I. Upon exiting region I, each light ray will have traveled an OPL $fDn_2 + (1-f)Dn_2$, or Dn_2.

Leaving region I, the reference beam continues traveling a distance $H_1 + D/2$ within the structure before reaching the bottom surface. Upon leaving the structure, the reference beam travels a distance H_2 through medium n_1 to reach the detector. The total OPL for the reference beam ($\mathrm{OPL}_{R,\mathrm{tot}}$) is therefore defined as

$$\begin{aligned}\mathrm{OPL}_{R,\mathrm{tot}} &= \mathrm{OPL}_{R,\mathrm{I}} + \mathrm{OPL}_{R,\mathrm{II}} + \mathrm{OPL}_{R,\mathrm{III}} + \mathrm{OPL}_{R,\mathrm{IV}}\\ &= D\cdot n_2 + H_1\cdot n_2 + \frac{D}{2}\cdot n_2 + H_2\cdot n_1,\\ \mathrm{OPL}_{R,\mathrm{tot}} &= \left(\frac{3}{2}D + H_1\right)n_2 + H_2 n_1. \end{aligned} \tag{1}$$

Derivation of the probe beam OPL in regions I and II is similar to that of the reference beam. Within region I, the probe beam travels an OPL Dn_2; within region II, the probe beam travels outside the SOHFI in refractive index n_1 for a distance H_1 resulting in an OPL of $H_1 n_1$.

In region III, however, the total OPL consists of two terms, since each probe ray travels outside *and* inside the SOHFI structure. After leaving region II, the distance a probe ray travels in medium n_1 before striking the slanted surface varies with the ray's lateral distance from the structure. Probe rays traveling close to the structure will strike the slanted surface and refract into the monolith immediately, but rays traveling further from the interferometer will re-enter the structure closer to the bottom of region III. Following the same logic used in region I, a probe ray will travel an OPL $\left(fD - \frac{D}{2}\right)n_1$ before reaching the slanted surface, where $f > 0.5$.

Given the constant slope of the slanted surface, the angle of incidence for each probe ray at the n_1:n_2 boundary is equal ($\theta_1 = 45°$). Therefore, the angle at which each probe ray refracts into the foot of the SOHFI (θ_2) is also equal, and is determined by Snell's law

$$n_1 \sin(\theta_1) = n_2 \sin(\theta_2) \therefore \theta_2 = \sin^{-1}\left(\frac{\sqrt{2}}{2}\frac{n_1}{n_2}\right). \tag{2}$$

The difference between the slant angle of the surface and θ_2 produces θ_3:

$$\theta_3 = 45° - \theta_2 = 45° - \sin^{-1}\left(\frac{\sqrt{2}}{2}\frac{n_1}{n_2}\right). \tag{3}$$

Furthermore, the distance a probe ray travels within the SOHFI in region III, t, is based on the height above the bottom surface at which the probe ray strikes the slanted surface, H_3. Based on the equivalence of the right isosceles triangles in region I and regions II and III, $H_3 = (1-f)D$. The geometric length t, then, is defined by Eq. (4):

$$\cos(\theta_3) = \frac{H_3}{t} \therefore t = \frac{(1-f)D}{\cos(45° - \theta_2)}, \tag{4}$$

and the total OPL for the probe ray in region III is described by Eq. (5):

$$\mathrm{OPL}_{P,\mathrm{III}} = \left(fD - \frac{D}{2}\right)n_1 + \left(\frac{(1-f)\cdot D}{\cos(45° - \theta_2)}\right)n_2. \tag{5}$$

Through alternate interior angles, θ_3 also defines the angle of incidence of the probe ray at the n_2:n_1 boundary located at the bottom of the SOHFI structure. Snell's law ($n_2 \cdot \sin(\theta_3) = n_1 \cdot \sin(\theta_4)$) is again used to find θ_4, the angle at which a probe ray will refract out of the bottom surface of the structure before propagating a distance s through medium n_1 to strike the detector. Equations (6) and (7) define θ_4 and the OPL of a probe beam traversing region IV:

$$\theta_4 = \sin^{-1}\left(\frac{n_2}{n_1}\sin(\theta_3)\right), \tag{6}$$

$$\mathrm{OPL}_{P,\mathrm{IV}} = \left(\frac{H_2}{\cos(\theta_4)}\right)n_1. \tag{7}$$

The total OPL for the probe beam is defined by Eq. (9):

$$\begin{aligned}\mathrm{OPL}_{P,\mathrm{tot}} &= \mathrm{OPL}_{R,\mathrm{I}} + \mathrm{OPL}_{P,\mathrm{II}} + \mathrm{OPL}_{P,\mathrm{III}} + \mathrm{OPL}_{P,\mathrm{IV}}\\ &= Dn_2 + H_1 n_1 + \left(fD - \frac{D}{2}\right)n_1\\ &\quad + \left(\frac{(1-f)D}{\cos(\theta_3)}\right)n_2 + \left(\frac{H_2}{\cos(\theta_4)}\right)n_1, \end{aligned} \tag{8}$$

$$\begin{aligned}\mathrm{OPL}_{P,\mathrm{tot}} &= \left(H_1 + D\left(f - \frac{1}{2}\right) + \frac{H_2}{\cos(\theta_4)}\right)n_1\\ a \quad &+ D\left(1 + \frac{1-f}{\cos(\theta_3)}\right)n_2. \end{aligned} \tag{9}$$

Closer examination of $\mathrm{OPL}_{R,\mathrm{tot}}$ and $\mathrm{OPL}_{P,\mathrm{tot}}$ reveals additional insight into the operation of the SOHFI in a real-world environment. In a closed setting where n_1 is constant, θ_2, θ_3, and θ_4 are also constant; $\mathrm{OPL}_{R,\mathrm{tot}}$ reduces to a constant value, and the difference between $\mathrm{OPL}_{R,\mathrm{tot}}$ and $\mathrm{OPL}_{P,\mathrm{tot}}$ varies as a function of f. In a fluctuating environment, temporal changes in n_1 will cause θ_2, θ_3, and θ_4 to change as well. Furthermore, deviations in θ_4 would cause the slope of the probe beam's wavefront to vary relative to the reference beam, shifting the fringe frequency of the interferogram [27].

In the proposed geometry, the refraction of the probe beam at the slanted interface in region III is directly connected to the

working principle of the proposed interferometer, rendering the OPL difference between the reference and probe beams insignificant in measuring the refractive index of the sample and solidifying the SOHFI's unique position among other widely known interferometer geometries.

4. NUMERICAL ANALYSIS

In real-world systems, the energy captured by the interferometer's detector is the summation of the coherent and incoherent irradiance received from the source and environment. To present a clearer characterization of the interferogram's sensitivity, however, this discussion will focus solely on coherent irradiance, and no attention will be given to the incoherent signal. Simulation-wise, separation of the coherent and incoherent signals is straightforward, since the analysis software allows users to explicitly choose which data they would like to analyze.

To numerically validate the SOHFI concept, a three-dimensional computer-aided design (CAD) model of the interferometer was constructed and imported into Ansys Zemax OpticStudio Pro 2022 R2.02. In addition to its ray tracing capabilities, OpticStudio tracks a large amount of information about each ray from the source to the detector. In turn, the detector is characterized by an array of pixels, each with a finite area. By combining data from each ray, OpticStudio is able to perform calculations on phase, intensity, polarization, and coherence on a ray-by-ray basis [28–30]. Separating the real and imaginary parts of each ray as they are traced throughout the simulation, for example, interference between many coherent rays can be easily simulated. Validation for each interaction is readily available in the literature and supporting documents [31,32].

Composed of $250 \times 1000 \times 500$ voxels along x, y, and z directions, the resulting volume was attributed with fused silica and contains dimension parameter values of $D = 4.24$ mm, $H_1 = 2.08$ mm, and $H_2 = 4.7$ mm, and a depth of 1.81 mm (into the page along the x axis). The source, interferometer, and detector are surrounded by air at standard temperature and pressure ($n_{\text{air}} = 1.00027$).

A pre-packaged non-sequential interferometry example, "Interference Example 2 - A Mach–Zehnder Interferometer," was used as the basis of the simulations. The SOHFI geometry was placed within the simulation and unnecessary components were removed, producing the layout illustrated in Fig. 3. While some default settings were kept [e.g., the source's initial 0° phase and polarization Jones vector ($J_x = 0$, $J_y = 1$)], others were changed to enhance the realism of the simulation.

For instance, the original monochromatic source within the simulation was replaced by a quasi-monochromatic source in an effort to mimic a commercial off-the-shelf (COTS) laser. The updated source is modeled as a Gaussian distribution to match the output of Integrated Optics' 1064 L-25B diode-pumped solid-state (DPSS) free-space laser. Defined by 200 data points, the simulated source's power spectrum is further characterized by a center wavelength of 1064.23 nm and a 0.025 nm full-width at half-maximum (FWHM). A comparison of the modeled spectrum and empirical data for the same source is shown in the inset of Fig. 3.

Based on the modified power spectrum, the coherence length (l_c) of the source was calculated according to Eq. (10) [33], and

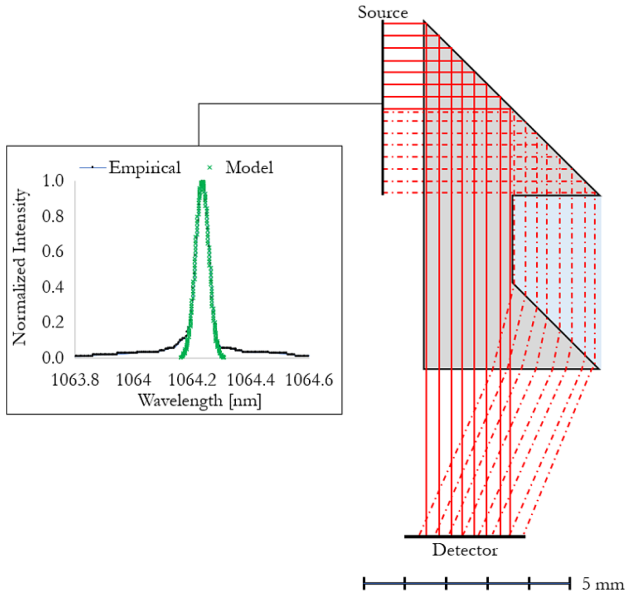

Fig. 3. Layout of the simulation; the inset compares the modeled quasi-monochromatic source to empirical data from the commercially available DPSS laser.

updated in the simulation:

$$l_c = \frac{\lambda^2}{n\Delta\lambda} = \frac{(1064.23 \times 10^{-9}\ \text{m})^2}{1.0003 \cdot (0.025 * 10^{-9}\ \text{m})} = 45.29\ \text{mm}. \quad \textbf{(10)}$$

In interferometric applications such as this, the coherence length of the source is especially important because it directly affects the contrast of the interference fringes. Although measurements are possible beyond the source's coherence length [34], fringe visibility in two-beam interferometer systems decreases as the OPL difference between the reference and probe beams becomes comparable to, or greater than, l_c. For the modeled quasi-monochromatic source, Eq. (10) predicts a coherence length of 45.29 mm, a typical l_c magnitude for non-single-longitudinal-mode (SLM) lasers.

Although tens of millimeters may seem short for practical applications, the short coherence length in this example further illustrates the advantage of the SOHFI's scalability since an interferometer in this configuration necessarily needs to be compact. For larger applications, a volume Bragg grating (VBG) can be used within the laser system to reduce the spectral linewidth to mere picometers, lengthening the source's coherence length beyond 1 m.

Changes to the source's spectral profile were supplemented with changes to its geometry. Specifically, the example's default point source and collimating lens were replaced by a perfectly collimated rectangular source sized to fit the input face of region I.

In a final modification, the SOHFI is configured to mimic a space-borne instrument in which the source, detector, and entry face of the interferometer are shielded from the external environment. Computationally, this was achieved by isolating the open-environment propagation region of the probe beam in regions II and III such that its refractive index can be changed independent of the background. Illustrated as a blue right trapezoid in Fig. 3, the refractive index of the isolated volume

is assumed to be spatially homogeneous. Isolating the volume, however, creates additional surfaces in the simulation. To mitigate unwanted reflections from the new volume, each of the new surfaces is defined as an ideal broadband anti-reflection coating.

In simulations, four billion rays from the collimated source travel through the SOHFI interferometer before striking the detector. Ideally, the size of the detector pixels would be modeled after an existing sensor. To avoid resolution issues, however, a pixel density of 64 million pixels per square millimeter was chosen based on a convergence study. The resulting detector comprises 960,000 pixels, ensuring an average of 4166 rays per pixel.

A. Two-Beam Interference

To demonstrate that the interferogram created by the SOHFI is the result of two-beam interference, two variations of the same simulation were performed. In the first simulation, the horizontal surface of the interferometer separating regions I and II was defined as a perfectly absorbing surface, disallowing the probe beam to travel to the detector. In the second simulation, the same horizontal surface was defined as a non-absorbing surface coated with a broadband anti-reflection coating. A comparison of the coherent irradiance for both simulations is illustrated in Fig. 4.

As expected, the coherent irradiance produced in the first simulation is unstructured and random and has no discernible fringes. When both beams are allowed to propagate through the SOHFI, the coherent irradiance is highly structured and contains fringes. As illustrated in the following section, the poor fringe definition of the latter case can be attributed to the relatively short coherence length of the source.

B. Fringe Visibility and Coherence Length

A third simulation was performed to demonstrate the impact of coherence length on fringe visibility. Leaving all other parameters unchanged, the coherence length of the source was increased to $l_c = 1$ m to mimic the use of a VBG-based DPSS free-space

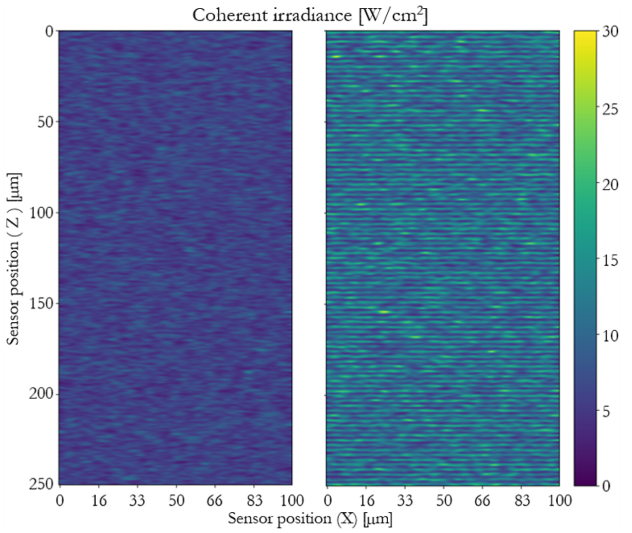

Fig. 4. Coherent irradiance is plotted for a SOHFI system with propagation of (left) only the reference beam and (right) reference and probe beams.

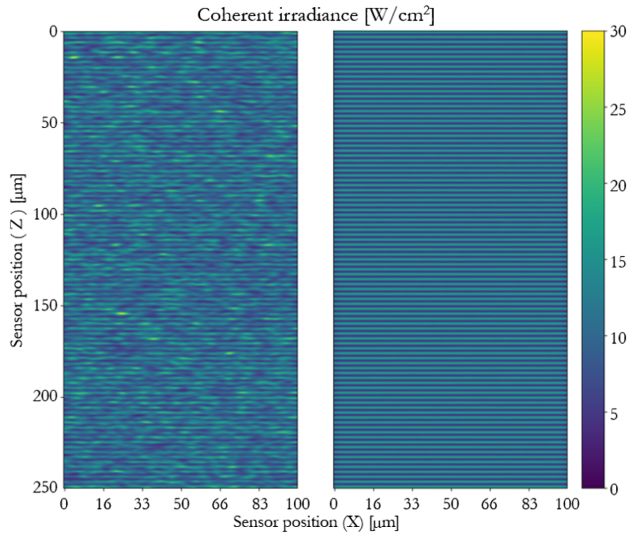

Fig. 5. Coherent irradiance is plotted for a SOHFI system with a source coherence length of (left) a 45.29 mm and (right) 1000 mm.

laser. The results, illustrated in Fig. 5, confirm the enhanced fringe definition since the overall strength of the fringes is increased while the fringe density remains constant. The low-frequency oscillation of the fringe amplitude seen in the latter plot is an artifact of the visualization and is not present in the numerical data.

Quantitatively, the "strength" of the fringes can be quantified by their visibility V using Eq. (11), where $I_{\max}$ and $I_{\min}$ represent the global maximum and minimum fringe intensities, respectively [35]:

$$V = \frac{I_{\max} - I_{\min}}{I_{\max} + I_{\min}}. \tag{11}$$

In the ideal case, complete destructive interference drives $I_{\min}$ to zero, resulting in a visibility of $V = 1$. In the simulated case of a source with $l_c = 1$ m, however, $I_{\min}$ and $I_{\max}$ were found to be 4.276 W/cm^2 and 17.22 W/cm^2, respectively, resulting in a fringe visibility of $V = 0.60$. Despite the calculated V value, however, the fringe visibility is expected to be much closer to unity based on the simulation geometry and the extremely long coherence length of the source.

Although fringe visibility characterization is highly applicable to conventional Mach–Zehnder interferometers, the same characterization of a SOHFI system is misleading. In the latter case, fringe visibility is expected to vary across the interferogram due to the dependence of the probe beam's OPL on f [Eq. (9)]. In practice, however, the variations in fringe visibility are not expected to significantly impact interferometric measurements due to the prevalence of fringe counting and image processing techniques.

C. Fringe Density versus Refractive Index

The relationship between fringe density and the refractive index witnessed by the probe beam was studied by modeling the isolated volume as a homogeneous block of water vapor—a choice designed to take advantage of existing refractive index

Table 1. Temperature (T), Pressure (P), Interpolated Refractive Index (n), and Fringe Density (lines/mm)

T [C]	P [MPa]	n	Lines/mm
380	0.1	1.00009	744
380	1.0	1.00094	736
420	10.0	1.01004	720
420	30.0	1.05750	656
400	30.0	1.10224	584
380	30.0	1.15348	512
400	100.0	1.19945	432
200	2.0	1.24862	360
0	100.0	1.29802	264

data over a wide variety of temperature and pressure combinations [36]. Within the existing measurements, however, refractive index values at the peak wavelength of the source (1.064 μm) are not available. Instead, measurements at the nearest two spectral values—1.01398 μm and 2.32542 μm—were linearly interpolated to estimate refractive index values for the water vapor at the appropriate wavelength. The values of temperature, pressure, and interpolated refractive index are listed in Table 1 alongside the resulting fringe densities.

As illustrated in Fig. 6, the relationship between fringe density and the refractive index of the isolated medium is highly linear ($R^2 = 0.9985$). Although the spatial frequency of the interferogram is determined by the angle θ_4 in Eq. (6), the results from this brief study help to numerically illustrate and validate the sensitivity of the interferogram's parameters to changes in the surrounding environment. From this relationship, relative changes in the refractive index can be predicted based on the number of interference fringes present on the detector.

D. Fringe Density versus Angular Misalignment

The interferogram fringe density is also affected by the alignment of the source to the SOHFI. For instance, as the structure is rotated in the y-z plane around its center, the source beam no longer enters region I orthogonal to the entry face. Instead, the refraction of the source beam across the interface causes a change in all other incidence angles of the reference and probe beams throughout the structure. At severe rotation angles, the incident beam no longer undergoes TIR from the slanted face in region I and begins to escape from the interferometer.

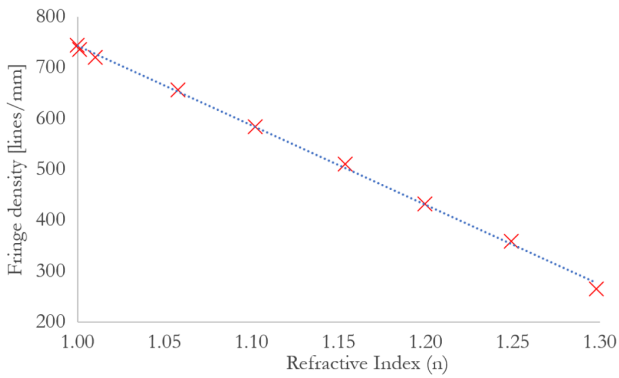

Fig. 6. Fringe density is plotted as a function of the refractive index of the volume traversed by the probe beam prior to re-entering the SOHFI. A linear fit to the data is shown in blue.

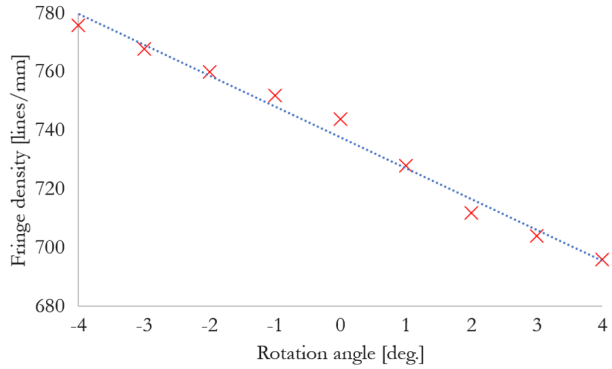

Fig. 7. Fringe density is plotted as a function of the rotation of the interferometer about the x axis. The blue dashed line plots a linear fit to the data points.

The rotational tolerance of the SOHFI design was examined by returning to the primary experiment layout detailed in the beginning of this section. Other than the rotation of the SOHFI, all other parameters were held constant. In each simulation, the SOHFI was rotated by 1° about its center in the y-z plane, and the number of fringes captured by the detector was recorded as a function of rotation angle. Although the results illustrated in Fig. 7 appear highly linear ($R^2 = 0.9854$), they also exhibit a sinusoidal oscillation due to changes in OPL induced by refraction of the input beam across the entry face.

The results demonstrate that the SOHFI design is capable of tolerating roughly 8° of angular misalignment—a value that can be identified and corrected through calibration since the relationship between fringe density and angular misalignment is known.

5. MANUFACTURABILITY

Despite its geometric simplicity, the proposed design of the interferometer may pose manufacturing challenges due to the dihedral angles produced at the intersection of regions I and II, and regions II and III.

One method to fabricate the proposed geometry may be to combine three optical components via index-matching adhesive or bonding. In this case, two of the components would represent the top and bottom isosceles right triangles. Equal in thickness to the two prisms, the shape of the third component depends on H_1; if $H_1 = \frac{D}{2}$, the tip of the lower triangle meets the bottom corner of the top triangle, and the third component takes the shape of a smaller triangular prism. Otherwise, if $H_1 > \frac{D}{2}$, the tip of the lower triangle is separated from the bottom corner of the top triangle, and the third component takes the shape of a right trapezoid. This align-and-bond technique may be time intensive, but the individual components are readily available.

On the other hand, high quality, large-scale production could be achieved using established optical manufacturing techniques such as laser or water jet cutting, mechanical grinding, diamond turning, and mold manufacturing. While diamond turning and other techniques enable rapid prototyping, the process places pressure on optical manufacturers to minimize surface roughness and alignment errors at each interface.

While the monolithic nature of the SOHFI provides distinct advantages, it is also limiting. The lack of moving parts

improves the overall manufacturability and mass production of the SOHFI, but the same lack of moving parts means the design is unable to perform phase-shifting interferometry, ultimately limiting the measurement resolution and the device's application space.

6. DISCUSSION

Based on the numerous advantages of the SOHFI concept, the design emerges as a promising new candidate for a wide variety of applications.

Due to its scalability, for instance, the same geometric design used in small applications (e.g., miniature gas analyzers) can also be used in large applications as well (e.g., hands-on classroom education). In this case, the analogy of how the interferometer operates in the classroom directly translates to how the same interferometer works in the field because TIR and refraction are scale independent. Similarly, the measurement resolution of the SOHFI is not affected by the structure's physical size, but instead depends on the wavelength of the incident source.

Furthermore, the design's use of TIR and refraction enable the device to be relatively insensitive to material composition and angular misalignment. In turn, the interferometer is able to take advantage of the mechanical, chemical, or thermal properties of the substrate that best fit the application at hand.

In real-world applications, caution must be taken to shield certain system components from unwanted ambient light. For example, using a bare source, interferometer, and detector (e.g., Fig. 3) would result in non-ideal measurements because ambient light would penetrate the broad side of the SOHFI and saturate the detector. For this reason, the source, detector, and reference portion of the interferometer would benefit from an opaque enclosure.

Additionally, the application space of the SOHFI can be extended via stacking. Although the interferometer's shape changes as a function of position in the y-z plane, the design is constant in the x direction. Therefore, a SOHFI geometry extruded along the x axis would be able to simultaneously utilize multiple collimated sources similarly aligned along the x axis. If each source were used with an accompanying detector (or one elongated detector capable of collecting the interferogram of each collimated source), one environment could be simultaneously probed with multiple wavelengths in real time without the need to decouple the received signals. In this configuration, each of the stacked interferometers is spatially offset from one another, and each individual SOHFI characterizes the refractive index at a different spatial location. Together, the collection of spatially separated measurements would enable characterization of a full three-dimensional space in real time.

Lastly, the usefulness of the SOHFI geometry appears to rely entirely on the coherence of the souce, but this is not entirely true. In the case that a coherent source cannot be found, the SOHFI structure could still function as an absorption spectrometer. Although interference will not occur without a coherent source, an incoherent collimated input beam placed in front of region I will still traverse the SOHFI structure, splitting into two beams and recombining at the detector. If the wavelength of the incoherent source is chosen such that it is highly absorbed by a specific environmental agent (e.g., a gas), the relative amplitudes of the reference and probe beams can be used to indicate the presence of the environmental agent within the surrounding environment.

The success of this configuration heavily relies on the user's ability to separately measure the amplitude of the reference and probe beams. Analytically, these quantities can be predicted given knowledge of the source and the SOHFI substrate material when no absorbing gas is present in region II. When the highly absorbing medium is introduced, the amplitude of the probe beam will decrease due to absorption, thereby reducing the total amplitude of the combined signal witnessed by the detector. Further, the analytical calculations can be empirically validated for both reference and probe beams prior to the introduction of the absorbing medium. Similar to the technique described in Section 4.A, the intensity of the reference beam arriving at the detector can be measured by placing an opaque layer on the horizontal surface dividing regions I and II, disallowing the probe beam to propagate through the remainder of the structure. Similarly, the intensity of the probe beam can be isolated and measured by placing an opaque mask on the upper portion of the entry face, thereby disallowing the reference beam to pass through the entry face.

7. CONCLUSION

This study describes a scalable optically homogeneous free-space interferometer. The first of its kind, the SOHFI structure is truly homogeneous and monolithic and has no moving parts or external elements. Each feature of the proposed design is significant, enabling the structure to be scalable, intuitive, versatile, and mechanically and optically robust. Through analytical and numerical validation, the relationships and tolerances of the SOHFI structure were shown for changes in the external refractive index and angular offset between the incident source and the monolithic structure. Coupled with the design's sensitivity to changes in the refractive index, the numerous advantages afforded by the SOHFI structure make it a prime candidate for applications in atmospheric sensing, passive chemical detection, and spaceborne technologies.

Disclosures. The author declares no conflicts of interest.

Data availability. No data were generated or analyzed in the presented research.

REFERENCES

1. F. Maurice, *Diverse Applications of Interference* (Academic, 1966).
2. P. Hariharan, *Basics of Interferometry* (Elsevier/Academic, 2007).
3. Y. Liu, H. Lin, Y. Dai, A. Zhou, and L. Yuan, "Fiber in-line Mach-Zehnder interferometer for gas pressure sensing," IEEE Sens. J. **18**, 8012–8016 (2018).
4. R. Kanawade, A. Kumar, D. Pawar, K. Vairagi, D. Late, S. Sarkar, R. K. Sinha, and S. Mondal, "Negative axicon tip-based fiber optic interferometer cavity sensor for volatile gas sensing," Opt. Express **27**, 7277–7290 (2019).
5. K. Nazeri, F. Ahmed, V. Ahsani, H.-E. Joe, C. Bradley, E. Toyserkani, and M. B. G. Jun, "Hollow-core photonic crystal fiber Mach-Zehnder interferometer for gas sensing," Sensors **20**, 2807 (2020).
6. Y. Cui, Y. Jiang, T. Liu, J. Hu, and L. Jiang, "A dual-cavity Fabry-Perot interferometric fiber-optic sensor for the simultaneous measurement of high-temperature and high-gas-pressure," IEEE Access **8**, 80582–80587 (2020).

7. N. Sabri, S. A. Aljunid, M. S. Salim, and S. Fouad, *Fiber Optic Sensors: Short Review and Applications* (Springer, 2015), pp. 299–312.
8. J. A. Buck, *Fundamentals of Optical Fibers*, 2nd ed. (Wiley, 2004).
9. J. A. Harrington, *Infrared Fibers and Their Applications* (SPIE, 2004).
10. J. B. Rafert, R. G. Sellar, and J. H. Blatt, "Monolithic Fourier-transform imaging spectrometer," Appl. Opt. **34**, 7228–7230 (1995).
11. Z. Bleier, C. Brouillette, and R. Carangelo, "A monolithic interferometer for FT-IR spectroscopy," Spectroscopy **14**, 46–49 (1999).
12. J. M. Harlander, F. L. Roesler, C. R. Englert, J. G. Cardon, R. R. Conway, C. M. Brown, and J. Wimperis, "Robust monolithic ultraviolet interferometer for the shimmer instrument on STPSAT-1," Appl. Opt. **42**, 2829–2834 (2003).
13. B. Hicks, T. Cook, B. Lane, and S. Chakrabarti, "Monolithic achromatic nulling interference coronagraph: design and performance," Appl. Opt. **48**, 4963–4977 (2009).
14. J. Herbst and P. Vrancken, "Design of a monolithic michelson interferometer for fringe imaging in a near-field, UV, direct-detection Doppler wind lidar," Appl. Opt. **55**, 6910–6929 (2016).
15. D. Wei, Y. Zhu, J. Liu, Q. Gong, M. Kaufmann, F. Olschewski, P. Knieling, J. Xu, R. Koppmann, and M. Riese, "Thermally stable monolithic Doppler asymmetric spatial heterodyne interferometer: optical design and laboratory performance," Opt. Express **28**, 19887–19900 (2020).
16. Š. Řeřucha, M. Holá, M. Šarbort, J. Hrabina, J. Oulehla, O. Číp, and J. Lazar, "Compact differential plane interferometer with in-axis mirror tilt detection," Opt. Laser Eng. **141**, 106568 (2021).
17. A. Waldron, A. Allen, A. Colón, J. C. Carter, and S. M. Angel, "A monolithic spatial heterodyne Raman spectrometer: initial tests," Appl. Spectrosc. **75**, 57–69 (2020).
18. H. Ichikawa, "Two-beam prism interferometer for noise-free fringe generation," Appl. Opt. **33**, 37–38 (1994).
19. C. Weigel, E. Markweg, L. Müller, M. Schulze, H. Gargouri, and M. Hoffmann, "A monolithic micro-optical interferometer deep etched into fused silica," Microelectron. Eng. **174**, 40–45 (2017), Micro/nano devices and systems edited by Roman Beigelbeck and Bernhard Jakoby.
20. E. R. Peck and S. W. Obetz, "Wavelength or length measurement by reversible fringe counting," J. Opt. Soc. Am. **43**, 505–509 (1953).
21. W. R. C. Rowley, "Some aspects of fringe counting in laser interferometers," IEEE Trans. Instrum. Meas. **15**, 146–149 (1966).
22. F. Barone, E. Calloni, R. D. Rosa, L. D. Fiore, F. Fusco, L. Milano, and G. Russo, "Fringe-counting technique used to lock a suspended interferometer," Appl. Opt. **33**, 1194–1197 (1994).
23. P. Křen and P. Balling, "Common path two-wavelength homodyne counting interferometer development," Meas. Sci. Technol. **20**, 084009 (2009).
24. M. S. Shumate, "Interferometric measurement of large indices of refraction," Appl. Opt. **5**, 327–331 (1966).
25. C. Sáinz, P. Jourdian, R. Escalona, and J. Calatroni, "Real time interferometric measurements of dispersion curves," Opt. Commun. **110**, 381–390 (1994).
26. S. R. Kachiraju and D. A. Gregory, "Determining the refractive index of liquids using a modified Michelson interferometer," Opt. Laser Technol. **44**, 2361–2365 (2012).
27. R. Smith and F. K. Fuss, "Theoretical analysis of interferometer wave front tilt and fringe radiant flux on a rectangular photodetector," Sensors **13**, 11861–11898 (2013).
28. M. Bass, *Handbook of Optics*, 2nd ed. (McGraw-Hill, 1995), vol. **1**.
29. R. R. Shannon, *The Art and Science of Optical Design* (Cambridge University, 1997).
30. Ansys, *Ansys Zemax OpticStudio User Manual* (2022).
31. N. Coluccelli, "Nonsequential modeling of laser diode stacks using Zemax: simulation, optimization, and experimental validation," Appl. Opt. **49**, 4237–4245 (2010).
32. L. Wang, A. M. Mahmoud, B. L. Anderson, D. D. Koch, and C. J. Roberts, "Total corneal power estimation: ray tracing method versus Gaussian optics formula," Invest. Ophthalmol. Visual Sci. **52**, 1716–1722 (2011).
33. W. T. Silfvast, *Laser Fundamentals*, 2nd ed. (Cambridge University, 2009).
34. Y. Salvadé, F. Przygodda, M. Rohner, A. Polster, Y. Meyer, S. Monnerat, O. Gloriod, M. Llera, R. Matthey, J. di Francesco, F. Gruet, and G. Mileti, "Interferometric measurements beyond the coherence length of the laser source," Opt. Express **24**, 21729–21743 (2016).
35. M. Born and E. Wolf, *Principles of Optics: Electromagnetic Theory of Propagation, Interference, and Diffraction of Light*, 7th ed. (Cambridge University, 2019).
36. P. Schiebener, J. Straub, J. M. H. L. Sengers, and J. S. Gallagher, "Refractive index of water and steam as function of wavelength, temperature and density," J. Phys. Chem. Ref. Data **19**, 677–717 (1990).